Landscape and Urban Planning 167 (2017) 212–224

Contents lists available at ScienceDirect

Landscape and Urban Planning

journal homepage: www.elsevier.com/locate/landurbplan

Research Paper

Urban morphology detection and computation for urban climate research

Yong Xu[a], Chao Ren[a,b,c,*], Peifeng Ma[d], Justin Ho[c], Weiwen Wang[b], Kevin Ka-Lun Lau[a,c,e], Hui Lin[d], Edward Ng[a,b,c]

[a] Institute of Future Cities, The Chinese University of Hong Kong, Shatin, NT, Hong Kong, China
[b] School of Architecture, The Chinese University of Hong Kong, Shatin, NT, Hong Kong, China
[c] Institute of Environment, Energy and Sustainability, The Chinese University of Hong Kong, Shatin, NT, Hong Kong, China
[d] Institute of Space and Earth Information Science, The Chinese University of Hong Kong, Shatin, NT, Hong Kong, China
[e] Jockey Club Institute of Ageing, The Chinese University of Hong Kong, Shatin, NT, Hong Kong, China

ARTICLE INFO

Keywords:
Urban morphological parameters
High-density cities
Urban planning
WUDAPT
Urban climatic map

ABSTRACT

Urban morphology information is an important indicator in urban planning, information management, and urban climatic applications. However, the problem of urban morphological data harmonization, quality, and availability are well-known, especially in developing countries. In this study, a novel satellite-based approach was proposed to extract 3D urban morphology information, and then retrieve and validate typical urban morphological parameters for urban climatic applications. Some most widely used urban morphological parameters—building coverage ratio (BCR), building height (BH), building volume density (BVD), frontal area index (FAI), sky view factor (SVF), and roughness length (RL)—were calculated and validated. Experiments conducted throughout the entire urban environment of Kowloon Peninsula, the most complex and high-density urban area in Hong Kong, demonstrated that all of the retrieved parameters had a high prediction accuracy, compared with the actual data at spatial resolutions of hundreds of meters. In particular, the prediction accuracy of BCR, BH, BVD, and RL was 70–80% while the accuracy of SVF and FAI was 80–90%. This set of urban morphological data is employed to generate a Hong Kong Urban Climatic Map. As an extension of the World Urban Database and Access Portal Tools (WUDAPT) method to provide 2D urban form data for cities worldwide, this newly developed method can quickly and efficiently produce highly accurate 3D urban morphology data for cities where actual urban morphology data are not accessible. This study also expands spatial understanding of urban climatic conditions in a fast and efficient way, enabling urban climatic application in urban planning for sustainable urban living.

1. Introduction

Urban development towards high-density or compact living is an irreversible trend of urbanization (UNFPA, 2015). Twenty-eight out of the world's 34 megacities are located in developing countries (Wendell Cox Consultancy, 2015). According to projections by the United Nations Population Division (UNFPA, 2015), nearly all future population growth will occur in developing countries; consequently, the number of megacities in developing countries will increase. However, due to this rapid urbanization, numerous climatic and environmental problems or degradations have arisen, such as air pollution and heat stress, which significantly affect public health in these areas (Grimmond, 2007). Simultaneously, these countries are the ones most affected by climate change (H & ppe, 2008, Chap. 2; Roth, 2007). However, there is a problem of urban morphological data harmonization, quality and availability, especially in developing countries and regions (Mills, Ching, See, Bechtel, & Foley, 2015).

Urban morphology can influence the local urban climate through morphological parameters (Middel, Häb, Brazel, Martin, & Guhathakurta, 2014; Stewart et al., 2012). In particular, urban areas with higher building density and more complex urban morphology exhibit more intense heat islands and lower permeability of urban air ventilation (Chen et al., 2012; Ng, Yuan, Chen, Ren, & Fung, 2011). Numerical simulations with weather research and forecasting (WRF) models have also indicated that better simulation results for air pollution and climate change scenarios can be achieved using more accurate urban morphological information (Chen et al., 2011; Salamanca, Martilli, Tewari, & Chen, 2011; Wang and Dai, 2015). Thus, high-quality urban morphological information is essential to improve understanding of urban morphological characteristics and

* Corresponding author at: Institute of Future Cities, The Chinese University of Hong Kong, Shatin, NT, Hong Kong, China.
E-mail addresses: xuyong@cuhk.edu.hk (Y. Xu), renchao@cuhk.edu.hk (C. Ren), peifengma1986@gmail.com (P. Ma), justinckho@gmail.com (J. Ho), kevinlau@cuhk.edu.hk (K.K.-L. Lau), huilin@cuhk.edu.hk (H. Lin), edwardng@cuhk.edu.hk (E. Ng).

http://dx.doi.org/10.1016/j.landurbplan.2017.06.018
Received 5 February 2016; Received in revised form 27 May 2017; Accepted 25 June 2017
Available online 08 July 2017

their impact on urban climate.

Due to a lack of comprehensive coverage and up-to-date urban morphological data for developing countries, poor quality urban studies and limited urban climatic applications are common (Wang and Dai, 2015; Yu, Liu, Wu, Hu, & Zhang, 2010). Given the comparatively larger-area coverage and the almost real-time acquisition mode, satellite data make it possible to provide updated urban morphology information (Wang and Dai, 2015; Xu, Ma, Ng, & Lin, 2015).

Hong Kong is one of the most densely built cities in the world. It is located in the Pearl River Delta Region of China, which is still experiencing rapid urbanization. Within the territory of Hong Kong, Kowloon Peninsula is located in the southern part of the main Chinese landmass. Within this region, tall buildings lining narrow streets form deep canyons, and irregular street orientations and building layouts further increase the complexity of urban morphology. Thus, the complete urban area of the Kowloon Peninsula has been selected as the case study for this paper.

The objective of this study is to: (1) define key urban morphological parameters with climatic implications and are often used by climatologists and planners; (2) develop a satellite-based method to derive three-dimensional (3D) urban morphological information using stereo and SAR satellite data, thus generating a set of key urban morphological parameters; (3) using that information, conduct a case study involving urban climatic mapping in the Kowloon Peninsula; and (4) further discuss the limitations and advantages of this method, as well as its implications for urban climatic studies and WUDAPT method levels 1 and 2.

2. Review

2.1. Urban morphology and urban climate

It is well known that urbanization has not only gradually changed land cover and urban form through construction works and urban sprawl, but has also affected urban climatic conditions (Grimmond, 2007). However, communication between urban planners and urban climatologists is limited due to their different working vocabularies (Eliasson, 2000; Ng, 2012; Mills et al., 2010). There is therefore a need to understand how urban morphology affects urban climate, and to translate scientific findings about urban climatic phenomena into design practice. Since the 1950s, climatologists have studied how the structure of cities—including city size, street design, canyon geometry, and green plot ratio—affects local micro-climatic conditions (Givoni, 1998; Krazter, 1956; Landsberg, 1970; Mills et al., 2015; Oke, 1973, 1981, 1984, 1988, 2003; Steeneveld, Koopmans, Heusinkveld, & Theeuwes, 2014).

The local climate zone (LCZ) scheme, developed by Stewart and Oke (2012), represents one recent effort in urban climatic application to link urban morphology and urban climatic conditions. A set of parameters was selected to define a site's LCZ class by its geometric and surface cover parameters; these include sky view factor, aspect ratio, building surface fraction, impervious surface fraction, pervious surface fraction, building height, and terrain roughness. Another popular urban climatic application study, 'urban climatic mapping studies' (Ng, Ren, & Katzschner, 2012; Ren, Ng, & Katzschner, 2011), has determined that building coverage ratio (BCR), building height (BH), building volume density (BVD), frontal area index (FAI), and sky view factor (SVF) were often selected as urban morphological parameters. By conducting both field measurements and simulation results in Hong Kong, the researchers found that both building coverage ratio (BCR), and frontal area index (FAI) can effectively reflect urban wind ventilation (Ng et al., 2011), while building volume density and sky view factor can reflect intra-urban air temperature (Chen et al., 2012). Moreover, mean wind speed over a city is significantly affected by the roughness length of urban surfaces (Hansen et al., 1993). Thus, these six key urban morphological parameters have been selected for this study. Their impact on urban climatic conditions (mainly thermal and wind aspects) is summarized below.

2.1.1. Sky view factor (SVF)

The SVF is an important indicator for urban heat islands (Chen et al., 2012; Gál, Lindberg, & Unger, 2009; Svensson, 2004). One study conducted by Chen et al. (2012) in the Hong Kong urban area showed that intra-urban temporal difference ΔT is negatively related to SVF, and a 10% reduction in SVF can increase temperature by 6–10% ΔT at a scale of several hundreds of meters. This finding is consistent with previous studies conducted by Svensson (2004) and Gál et al. (2009) in Göteborg, Sweden and in Szeged, Hungary, respectively.

2.1.2. Frontal area index (FAI)

FAI is closely related to urban ventilation at pedestrian level. A study conducted by Ng et al. (2011) in the Hong Kong urban area showed that a 10% increase in FAI can produce a decrease of approximately 2.5% in wind velocity ratio at pedestrian level on a spatial scale of hundreds of meters. Thus, an average difference of 0.1 in the FAI value between satellite-derived and actual FAIs at the same spatial scale may translate to a wind velocity ratio difference of 0.025, and this difference corresponds to a pedestrian-level wind speed difference of 0.28 m/s (11 m/s * 0.025 = 0.28 m/s), given that the mean prevailing wind speed at 500 m height of this study area is 11 m/s (Yuan and Ng, 2012). A similar relationship was found by Razak, Hagishima, Ikegaya, and Tanimoto (2013) for high-density urban scenarios.

2.1.3. Building coverage ratio (BCR)

BCR is a useful indicator describing urban heat island intensity and the impact of built-up areas on local wind velocity ratios (Kubota, Miura, Tominaga, & Mochida, 2008). Results of Yoshie's wind tunnel test on the wind situation of selected urban areas of Tokyo and Hong Kong have confirmed an inversely proportional relationship between gross BCR and wind velocity ratio (Yoshie, Mochida, & Tominaga, 2006). That is, the higher the gross BCR, the lower the observable wind velocity ratio. Furthermore, Ng et al. (2011) have formulated a quantitative understanding of the impact of gross BCR on wind velocity ratio.

2.1.4. Building height (BH)

BH is a widely-used building morphology indicator in urban canopy models, in which different land use types can be parameterized with different heights (Ching, 2013). Numerical experiments and analytical models have confirmed that the impact of building height on wind speed is significant (Coceal and Belcher, 2005). One case study conducted at Hong Kong indicated that controlling building heights effectively promotes air ventilation in low/medium density areas (Ng et al., 2011). Other than the impact on wind speed, building height information also helps to describe the thermal properties of different buildings to better model anthropogenic heat for urban climate studies (Salamanca et al., 2011).

2.1.5. Building volume density (BVD)

High-density, built-up areas not only increase localized heat capacity (i.e., thermal load), but also reduce SVF values (Givoni, 1998; Oke, 1981). This is because the long-wave radiation can be blocked, and the energy released more slowly back into the sky. Therefore, the cooling process within a city center tends to be slower than in surrounding areas, producing higher temperatures within city centers. BVD is an indicator which represents the building density of the built-up areas. Chen et al.'s study (2012) of the Hong Kong urban area examined the impact of SVF and BVD on the local thermal environment.

2.1.6. Roughness length (RL)

RL is an important parameter in atmospheric models, associating the turbulent exchange process with surface roughness; it can

effectively determine wind velocity values over surfaces. Given that calculation of the RL index is complex and the data requirements are high, Hansen (1993) summarized the relationship between land-use categories (e.g., trees, rural, grass, and forest) with their RL values for engineering practice. Based on associations between different land-use categories and their RL values, Ren et al. (2012) evaluated climatic characteristics of different RL categories with land use information, applying the results to urban climate studies for compact cities.

2.2. Retrieval of urban morphology

In this study, the term "urban morphology" reflects only the physical characteristics of urban forms, such as building height, size, density, and pattern. A review of the relevant literature reveals two types of methods available for obtaining urban morphological information: conventional field measurement and satellite-based (Yu et al., 2010). Field measurement is the most common method for obtaining urban morphological data; it can be implemented quickly and easily, and is highly accurate for small study areas. However, this method is time-consuming and labor-intensive.

Compared with conventional manual methods, satellite technology is a fast and economical method for obtaining urban morphological information over large areas. According to available satellite data, there are three morphology extraction technologies: optical satellite images; synthetic aperture radar (SAR); and light detection and ranging data (LiDAR). However, each has its limitations. Optical images tend to suffer low prediction accuracy in retrieving the heights of tall buildings, limiting their application to high-density urban areas (Eckert and Hollands, 2010; Zeng, Wang, Zhan, Shi, & Gambles, 2014). SAR interferometry can provide only limited results (noisy and incomplete data), especially for high-density urban areas where the mutual inference of surrounding buildings is significant (Colin-Koeniguer and Trouve, 2014; Sportouche, Tupin, & Denise, 2011). LiDAR can provide satisfactory results, but is expensive, and flight plan restrictions limit its application in large urban areas (Burian, Velugubantla, & Brown, 2002; Zhou and Zhou, 2014). These difficulties restrict the practical use of single satellite data for 3D building retrieval in large urban areas, especially in high-density areas with complex scenarios (Xu et al., 2015).

Several studies have achieved promising results after attempting to integrate different data sources—such as SAR and optical image fusion, and LiDAR and optical image fusion— for 3D building retrieval (Sportouche et al., 2011; Wegner, Ziehn, & Soergel, 2014; Zhou and Zhou, 2014). However, most of the fusion approaches have used optical images to retrieve building footprints instead of building heights, and height information from optical images has not been fully exploited (Xu et al., 2015). Therefore, in this study, we present a new satellite-based method for deriving high-quality 3D urban morphological information, using both high-resolution stereo and SAR data, in which the advantages of both datasets in retrieving building footprints and heights are exploited and combined.

3. A novel satellite-based method to obtain urban morphology

In this study, a new satellite-based method is proposed to derive 3D building information using high-resolution stereo satellite data and SAR data. Based on that information, key urban morphological parameters will then be retrieved and validated for urban climate studies.

3.1. Satellite-based 3D building extraction

The approach was implemented using stereo images and multi-temporal SAR images as the inputs (Fig. 1), and included two main stages. First, building footprints were extracted from high-resolution satellite images using object-oriented classification technology. Next, building heights were estimated using an object-based height fusion approach in which initial height estimates from the stereo and multi-temporal SAR images were combined.

3.1.1. Building footprint extraction

The object-oriented classification method provided in Salehi, Zhang, Zhong, & Dey (2012) was used to extract initial building footprints through building texture, spectral, and height information. In the proposed method, all of the objects in the image were extracted as potential building candidates, and most of the non-building objects (e.g., water, vegetation, roads) were then removed through a process of elimination. The remaining objects reflected the building footprints. This procedure involved the following steps.

First, a multi-scale, object-oriented segmentation approach was used to obtain image objects, in which original satellite data was segmented into homogeneous objects based on certain criteria, like scale, spectral, and spatial information. After initial segmentation, certain small objects were further merged with the objects surrounding them according to their spectral differences. This step was conducted using an object-oriented segmentation tool implemented in eCognition. Second, some of the non-building classes (e.g., vegetation and shadow) were removed from the obtained objects using the normalized difference vegetation index (NDVI) and the shadow index (Salehi et al., 2012). Third, non-building classes (e.g., roads) with different shape indices were removed from the remaining objects using the shape and width/height ratio indices. Finally, non-building classes with heights similar to the nearby ground (e.g., bare land) were removed from the remaining objects using the height model from stereo images; this was because the heights of buildings tended to exceed those of the nearby ground. The obtained objects were further processed using mathematical morphology operations to eliminate spurious objects, and the remaining objects were accepted as the building footprints.

3.1.2. Building height extraction

In this stage, building heights were estimated and assigned to each building footprint in two steps. First, two initial building height estimates were extracted from the stereo and SAR images. For the stereo images, an empirical model was used to extract the building height estimates using the built-in rational polynomial coefficient (d'Angelo, Lehner, Krauss, Hoja, & Reinartz, 2008). For the multi-temporal TerraSAR images, the TomoSAR technique was used to derive the vertical heights of the scatters (Ma, Lin, Lan, & Chen, 2015). Second, the initial building height estimates were combined, using an object-based fusion approach to generate a fused result for the same building footprint (Xu et al., 2015).

For example, Fig. 2(a) and (b) shows two initial building height estimates obtained from stereo images and multi-temporal SAR images, while Fig. 2(c) shows the buildings whose heights are to be estimated. The height estimates from the stereo images cover all of the study area, whereas the SAR height estimates tend to have missing data due to noise and distortion of SAR data. Moreover, SAR results tend to include substantial positioning errors, affecting the correct pairing of buildings and height information.

To reduce the effect of SAR positioning error on the estimation of building height, a novel object-based fusion approach was proposed and used to extract building heights using SAR height estimates (Fig. 2) in three stages. First, SAR height points were organized as objects using the connection component analysis method. Second, SAR height objects were matched with the nearest building footprints based on their overlapping areas. Third, for all matched footprints, heights were assigned using the maximum value of the matching SAR height points. As Fig. 2(e) shows, two SAR objects were highlighted with green and red colors, and their matched buildings were buildings A and B.

For each footprint, two height results can be obtained using the height estimates from stereo and SAR images. However, the height results can be combined based on their differences. If there is a large difference, the higher value represents the fused result. Otherwise, the

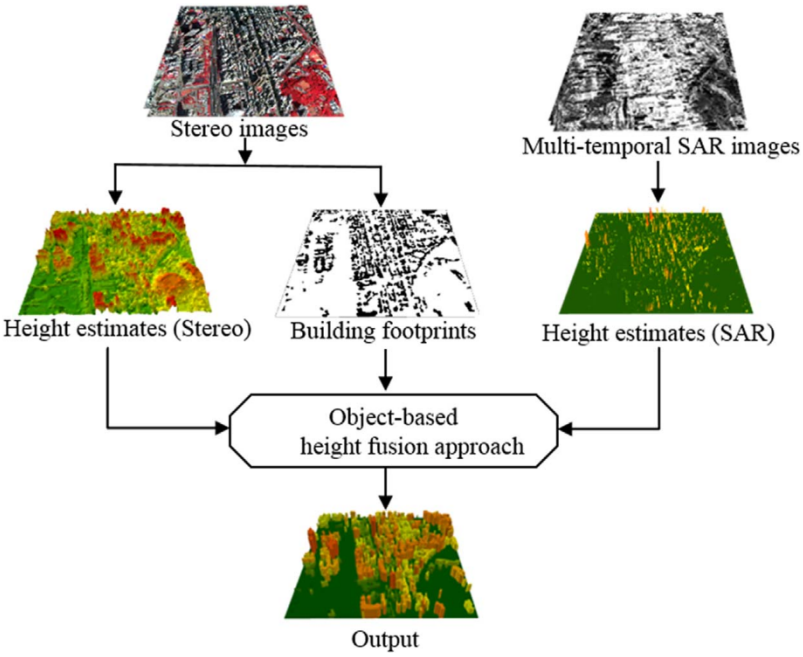

Fig. 1. Procedure of the proposed approach for 3D building extraction.

average is the fused result. As Fig. 2(f) shows, building A had a final height result of 76 m (a value higher than both results), while building B had a final height result of 46 m, which is the average value of both results. For some buildings without SAR height estimations, height results obtained from stereo images were assigned to them.

3.2. Derivation of urban morphological parameters

A set of urban morphological parameters was then calculated according to the 3D building information from the satellite data. The morphological parameters tested included BCR, BH, BVD, SVF, FAI, and RL.

3.2.1. Building coverage ratio

The BCR reflects a building's footprint area over the site's area (Yu et al., 2010). As Fig. 3(a) shows, it is calculated as:

$$\mathrm{BCR} = \frac{\sum_{i=1}^{N} C_i}{S_L} \tag{1}$$

where C_i reflects the coverage area of building i, S_L is the size of the land lot, and N is the total number of buildings on the land lot. Importantly, the number of buildings (N) can be different from satellite data to actual data within the same land lot, and the land lot size should be fixed with hundreds of square meters for validation. Six different land lot sizes have been tested in this study, including 100*100 m^2, 200*200 m^2, 300*300 m^2, 400*400 m^2, 500 *500 m^2, and 600*600 m^2. Further details of the sensitivity of land lot sizes are discussed in section 6.2. Unless otherwise specified, definitions of N and S_L are the same for

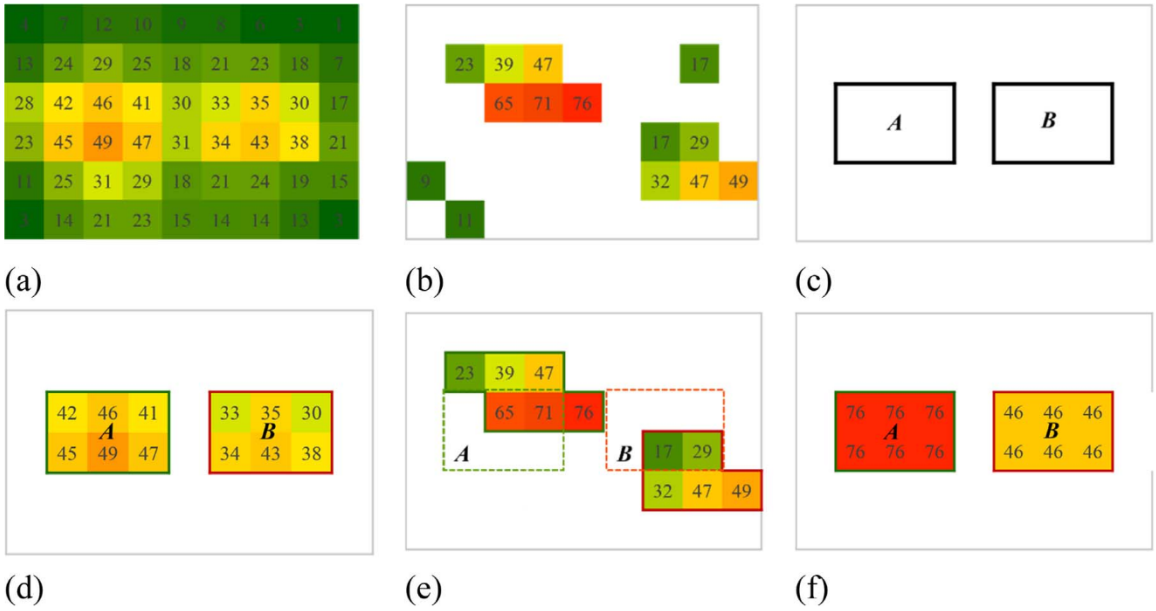

Fig. 2. Object-based fusion approach for building height retrieval: (a) initial height estimates using stereo images (unit: meters); (b) initial height estimates using SAR images (unit: meters); (c) final building footprints; (d) extracted height points for selected buildings (stereo); (e) extracted SAR height points as objects for selected buildings (SAR); (f) fused heights of buildings.

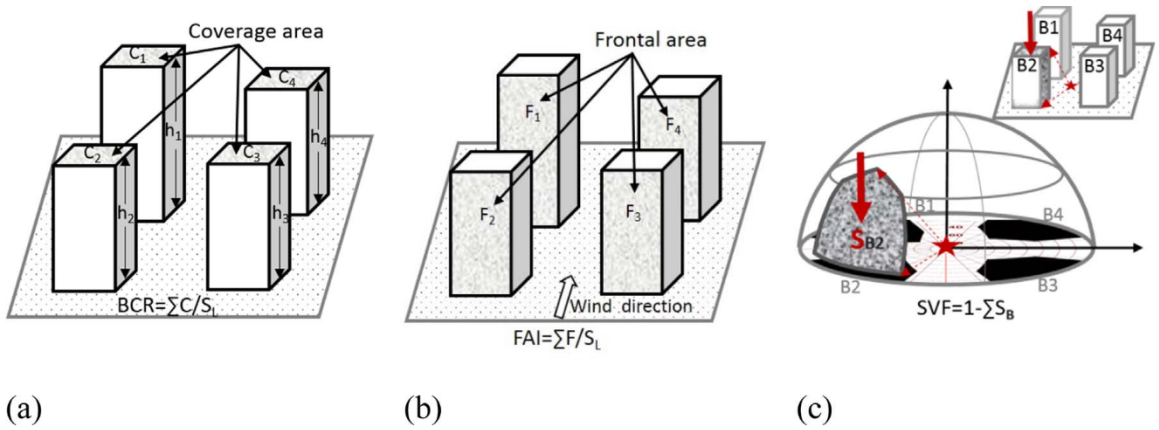

Fig. 3. Illustrated calculation of BCR, FAI, and SVF: (a) BCR, (b) FAI, and (c) SVF.

the other morphological parameters. Once the building footprints on a certain land lot are obtained, then the BCR for that lot can be calculated.

3.2.2. Building height

In this study, BH refers to the area averaged building height (Salamanca et al., 2011), calculated as:

$$\mathrm{BH} = \frac{\sum_{i=1}^{N} (C_i \times h_i)}{\sum_{i=1}^{N} C_i} \tag{2}$$

where C_i reflects the coverage area of building i, h_i is its height, N is the total number of buildings on a land lot.

3.2.3. Building volume density

BVD is an index to quantify the building density over a site's area (Petralli, Massetti, Brandani, & Orlandini, 2014), calculated as:

$$\mathrm{BVD} = \frac{\sum_{i=1}^{N} (C_i \times h_i)}{S_L} \tag{3}$$

where C_i reflects the coverage area of building I, h_i is the height of building i, S_L is the size of the land lot, and N is the total number of buildings on that lot. Formula (3) (see above) indicated that the value of BVD is highly dependent on the size of the land lot (S_L), and its unit is $m^3\,m^{-2}$.

3.2.4. Sky view factor

SVF measures the degree to which the sky is obscured by the surroundings at a given point (Grimmond, Potter, Zutter, & Souch, 2001). SVF value is between 0 and 1, with a value of 0 meaning that all outgoing radiation is totally obscured and a value of 1 meaning that all radiation can dissipate freely into the sky. Estimation of SVF is assumed to be the sum of the angle element that reaches the visible sky in the entire hemispheric environment. In this study, SVF was calculated utilizing the method described in Matuschek and Matzarakis (2010). As Fig. 3(c) shows, it is calculated as:

$$\mathrm{SVF} = 1 - \sum_{i=1}^{n} \sin^2\beta_i \left(\frac{\alpha_i}{360^o}\right) \tag{4}$$

where n reflects the total number of the angle elements of the obstacles in the hemispheric environment and α_i and β_i reflect the elevation and azimuth angles of the angle element i, respectively.

3.2.5. Frontal area index

FAI refers to a building's frontal area over a site's area, calculated by summarizing the former over the latter in a certain wind direction (Ng et al., 2011). As Fig. 3(b) shows, the FAI in one direction is calculated as:

$$\mathrm{FAI}(\theta) = \frac{\sum_{i} F_i(\theta)}{S_L} \tag{5}$$

where $F_i(\theta)$ represents the frontal area of building i in wind direction θ, and S_L is the size of the land lot for the study area.

3.2.6. Roughness length

RL reflects how effective a surface area is in transforming the energy of the average wind, flowing over it, into turbulent motion in the boundary layer above (Gál and Unger, 2009).

In this study, an improved RL extraction approach with a 3D urban dataset provided in Macdonald, Griffiths, and Hall (1998) was used to calculate z_0. The basic model is:

$$\mathrm{RL} = H \times \frac{C_D}{0.74} \times (1 - \frac{z_d}{H})^2 \times \frac{FAI}{BCR} \tag{6}$$

where H is the volumetrically averaged building height, C_d is the obstacle drag coefficient, Z_d is the zero displacement height, FAI is the frontal area index, and BCR is the building coverage ratio.

The computation of the volumetrically averaged building and zeros displacement heights (H and Z_d) is performed as follows:

$$H = \frac{\sum_{i=1}^{N} v_i \times h_i}{\sum_{i=1}^{N} v_i} \tag{7}$$

$$z_d = H \times (1 + A^{-BCR} \times (BCR - 1)) \quad (8)$$

where v_i and h_i reflect the volume and height of building I, N is the total number of buildings in the site's area, A is a constant to control the convexity of the curve for displacement height, and BCR is the building coverage ratio.

As recommended by Macdonald et al. (1998), the obstacle drag coefficient C_d and the constant A for controlling the displacement height curve used in this study were set to 1.2 and 4, respectively.

3.3. Validation

For this study, actual parameters from a real 3D urban model were used—including 2D building footprints and building heights from local government (actual observations)—to validate the estimated parameters from the satellite images (estimated results). Two quantitative indices—the average absolute difference and the correlation coefficient

(CC) between estimated results and actual observations—were used to assess the quality of the prediction results using our proposed method. The computations of both indices are given below:

$$AAD = \frac{1}{n}\sum_{i=1}^{n}|y_i - x_i| \tag{9}$$

$$CC = \frac{n\sum xy - (\sum x)(\sum y)}{\sqrt{(n\sum x^2) - (\sum x)^2} \times \sqrt{(n\sum y^2) - (\sum y)^2}} \tag{10}$$

where y_i and x_i reflect the estimated and actual morphological parameter at location i, n is the total number of the testing samples.

The smaller average absolute difference (AAD) or percentage AAD value and higher CC reflect better prediction results. Moreover, a linear regression analysis was used to model the relationship between the prediction and the actual observations, so that the quantitative relationships between the estimated and actual parameters can be built for practical usage when the actual GIS data is not available. Herein, the goodness of fit statistics of R square and root mean square error (RMSE) were used to indicate the quality of the regression model. The higher R square and a smaller RMSE reflect a better-fit model.

4. Case study

4.1. Study area

The study area was located in the Kowloon Peninsula of Hong Kong (22N, 114E) (Fig. 4), a high-density urban area with an average building height of over 40 m, with some buildings reaching several hundred meters. Hong Kong, home to 7.5 million inhabitants, consists of a group of islands and a peninsula covering 1000 km^2. The city has a hilly topography, and only 25% of the land is developed (Ng, 2009). Due to limited land resources and high land prices, Hong Kong's property developers prefer to build taller, bulkier buildings with higher building plot ratios (e.g., 8–10 for some areas). As a result of its high density, Hong Kong is now suffering from the degradation associated with urban climate issues, such as urban heat islands and weak urban wind ventilation (HKPD, 2012).

4.2. Urban climate mapping

Urban Climatic Map (UCMap) is an urban climatic application tool for sustainable development, in which urban climate information is clearly and easily presented to urban planners during the implementation of the planning process (Acero, Arrizabalaga, Kupski, & Katzschner, 2013; Ren et al., 2011). More than 30 countries and 50 cities worldwide have developed their own UCMap studies and relevant applications (Ren et al., 2011). In Hong Kong, a feasibility study of the UCMap (2006–2012) was commissioned by the Planning Department of the Hong Kong SAR Government (HKPD, 2012). The original Hong Kong UCMap was developed using climate-relevant land use, along with building and topographical data from the local government. Specifically, six climate-relevant parameters—building volume, topography, green space, ground coverage, natural landscape, and proximity to openness—were used to generate an urban climate analysis map (HKPD, 2012; Ng et al., 2012).

In this study, we aim to generate a satellite-derived UCMap using the satellite-derived urban morphology in lieu of actual building morphology data. The procedure proposed by Ng et al. (HKPD, 2012) was adopted to generate the satellite-based UCMap. Two building- related parameters (building volume and ground coverage) were derived from satellite data, while the other four parameters were replicated from the original GIS-based UCMap. Finally, the satellite-derived UCMap was validated by comparing it with the original GIS-based result.

4.3. Input data

Within the study area, we obtained the actual building data (including two-dimensional building footprints and building height information) from 2010, along with the actual GIS data including vegetation (includes grass, woodland and forest) and open space data from year 2009. The acquired satellite data in this study area include the 14 TerraSAR-X images from 2011 and a pair of World-view2 stereo images from 2014; the TerraSAR images have a spatial resolution of 3m, and the World-view2 multi-spectral images have a spatial resolution of 2m. To ensure both datasets were comparable, Terra-SAR images were resampled into 2m. The satellite images, including TerraSAR and World-view2 images, were used to retrieve 3D building information employing

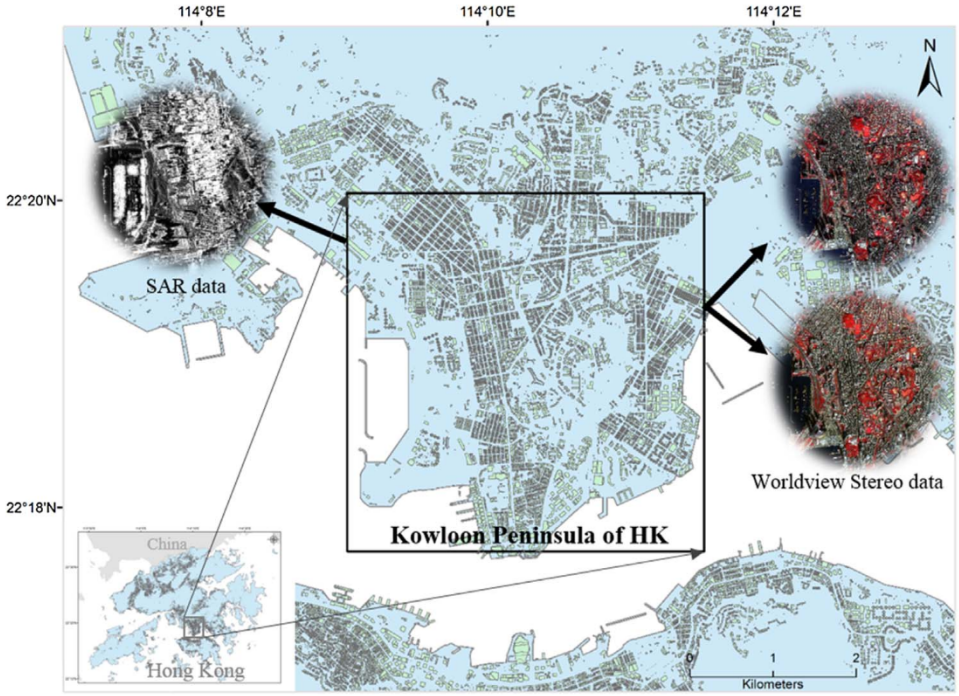

Fig. 4. Study area of Hong Kong.

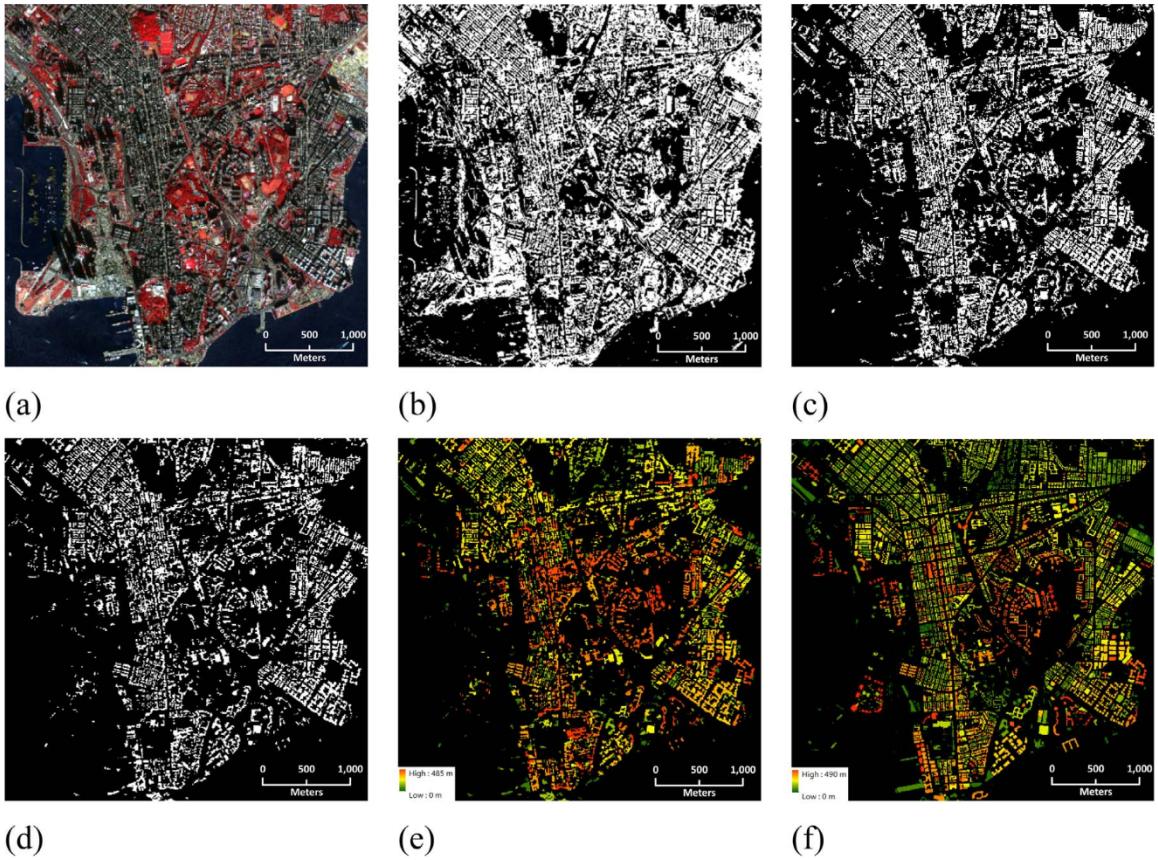

Fig. 5. 3D building extraction achieved using the proposed approach: (a) high-resolution satellite image; (b) preliminary objects extracted using the object-oriented classification process; (c) filtered result with low-height objects removed; (d) extracted building footprints; (e) building footprints and heights extracted using the proposed approach, and (f) actual 3D building information for comparison.

the proposed building extraction technique. The actual 3D building information from the Hong Kong Planning Department in 2010 was used as validation data. Based on the retrieved building morphology from satellite data, several representative morphological parameters, including BCR, BH, BVD, FAI, SVF, and RL, were generated and validated for urban climate studies.

5. Result and validations

5.1. Satellite-derived urban morphological parameters

SAR and stereo images were used to extract the 3D building model. Fig. 5(a) shows the high-resolution satellite data, while Fig. 5(b) shows the preliminary building footprints from Fig. 5(a), arrived at using the method introduced in Section 3.1. Fig. 5(c) shows the filtered building footprints after removing some bare land with lower height. Fig. 5(d) shows the refined building footprint results, calculated using morphology operations to fill various holes and eliminate spurious objects. Fig. 5(e) shows the final extracted buildings along with their heights, which were estimated from both the stereo and the SAR images using the approach proposed in Xu et al. (2015). The actual building information is provided in Fig. 5(f) for comparison.

Based on the extracted 3D model, a set of urban morphological parameters was calculated (estimated results). Setting the spatial resolution at 100 m, the six estimated urban morphological parameters—BCR, BH, BVD, SVF, FAI, and RL (Figs. 6(a)–(f))—were obtained pixel by pixel. For comparison purposes, the actual morphological parameters from the real 3D model (actual observations) are provided in Figs. 6(g)–(l), while the differences between the actual and the estimated parameters are shown in Figs. 6(m)–(r).

Two quantitative indices—the average absolute difference and the CC between the prediction results and actual observations—were used to assess the quality of the estimated results. The smaller AAD or percentage AAD value and a higher correlation coefficient reflect better estimation results. The correlation coefficient value was between 0 and 1. Table 1 shows the accuracy statistics of all the indices at a spatial resolution of 300 m, from which we can observe that all of the estimated results had high correlation coefficients (above 0.8) with the actual observations, and almost all of the satellite-derived parameters had relatively low-percentage AAD values (below 0.3).

Scatterplots were also produced for all results, where x-coordinates represent actual morphological parameters and y-coordinates represent estimated parameters from the satellite data. Fig. 7(a)–(f) presents the scatterplots for the six testing parameters, respectively. All scattering data were close to the 1–1 line, indicating that the variables estimated using satellite-based approach were similar to the actual morphological information. Visual inspection of the estimated and actual results in Fig. 6 also confirms the similarity.

To obtain the quantitative relationships between the estimated and actual parameters, a linear regression analysis was used to model the relationship between the predictions and the actual observations. Table 2 shows the built linear regression functions for all

of the validated parameters, which demonstrated that all estimated parameters had strong linear relationships with their actual values. The root-mean-square error of the estimated parameters were obtained based on the regression model: BCR, BH, BVD, SVF, FAI, and RL were 0.05, 11.8, 3.07, 0.07, 0.1, and 1.62, respectively. R squares between the prediction and the actual parameters of BCR, BH, BVD, SVF, FAI,

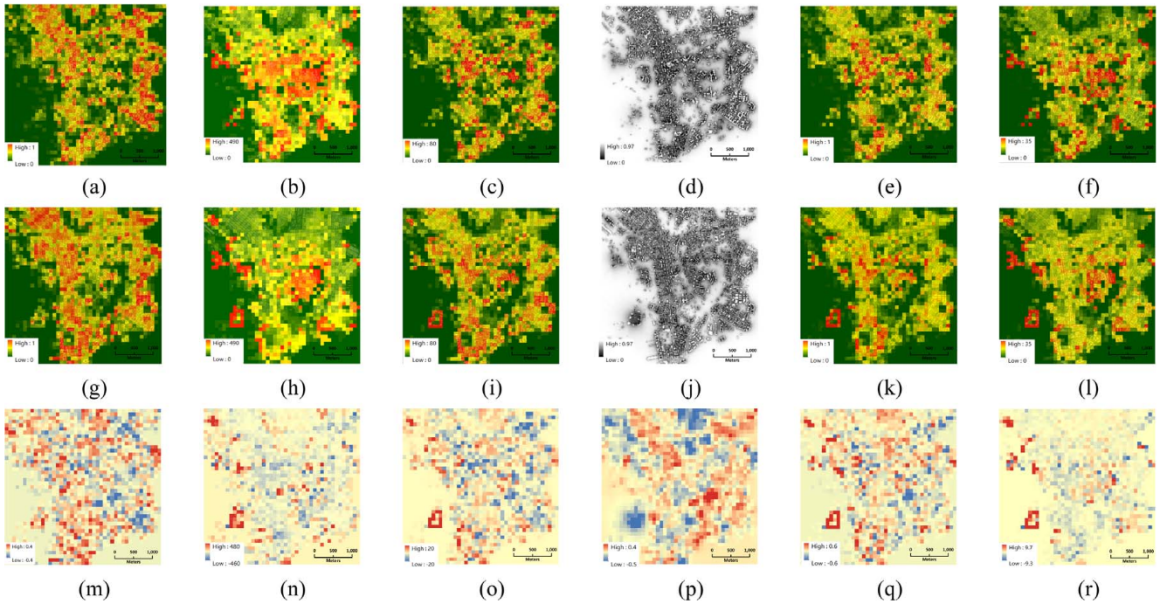

Fig. 6. Extraction of urban morphological parameters using the 3D building model. The upper row shows the results from the satellite data: (a) BCR; (b) BH; (c) BVD; (d) SVF; (e) FAI, and (f) RL. The middle row shows the results from the actual 3D data: (g) BCR; (h) BH; (i) BVD; (j) SVF; (k) FAI, and (l) RL. The lower row shows the difference between the actual and the estimated parameters: (m) BCR; (n) BH; (o) BVD; (p) SVF; (q) FAI, and (r) RL.

Table 1
Average absolute difference (AAD) and correlation coefficients (CC) between the satellite-derived urban morphological parameters and the actual parameters (average size: 300 m *300 m) from a real 3D urban model.

Parameters	BCR	BH	BVD	SVF	FAI	RL
Mean_value	0.18	43.4	8.28	0.63	0.32	5.16
CC	0.91	0.88	0.82	0.96	0.91	0.81
AAD	0.04	10.8	2.21	0.06	0.07	1.57
(*Percentage_AAD*[a])	*(22%)*	*(24%)*	*(27%)*	*(9%)*	*(22%)*	*(30%)*

[a] Percentage_AAD: the average absolute difference (AAD) divided by the mean value.

and RL were 0.85, 0.79, 0.80, 0.91, 0.87, and 0.66, respectively.

5.2. Satellite-based urban climatic map

Based on the derived building morphology, the procedure proposed by Ng et al. (HKPD, 2012) was followed to generate a satellite-based UCMap (Fig. 8). Two building-related parameters— building volume and coverage ratio—were obtained from the satellite data, while the other four parameters—topographical height, vegetation percentages, woodland/forest percentages, and proximity to open space—were from the actual GIS data. To validate the result, the generated result was compared with the original Hong Kong UCMap obtained from actual GIS data (Fig. 9).

Two quantitative indices, including the AAD and the CC, were calculated to assess the quality of the satellite-based UCMap. As shown in Table 3, it can be observed that the satellite-derived urban climatic map had a low-percentage AAD value of 14% and high correlation coefficient of 0.88. These results show that the satellite-derived UCMap from satellite data is consistent with the UCMap from actual GIS data.

A scatter plot was produced for the estimated result, with the x-coordinates representing the actual GIS-based UCMap and the y-coordinates representing the satellite-derived UCMap. Fig. 10 shows the scatter plot, in which all fall points along the 1:1 line, indicating that the estimated result is consistent with actual observations. Furthermore, a regression model was used to obtain the quantitative relationship between the satellite-derived results and the actual observations. The R square of the fitting model is 0.77 and the fitting gain is 0.91. These results also show that the satellite-derived UCMap from the satellite data is highly consistent with the result developed from the actual GIS data.

6. Discussion

6.1. Performance analysis

The above results and accuracy analysis support the following three findings. First, all of the urban morphological parameters retrieved from the satellite data had a high prediction accuracy. Overall, prediction errors for the validated parameters (300mx300m) were below 30%, meaning that more than 70% of the actual values were correctly estimated using the satellite data. Apart from prediction errors in terms of percentage AAD, all of the validated parameters had high correlation coefficients with the actual observations (above 0.8).

Second, among the parameters studied, SVF performed best, followed by FAI, BCR, BH, BVD, and RL. In particular, the prediction accuracy of SVF and FAI (93% and 82% via the regression model, respectively) was much better than the overall accuracy of BCR, BH, BVD, and RL (79%, 78%, 74%, and 68%, respectively). The superior performance of SVF and FAI is attributed to the fact that they are indirect parameters that are less dependent on building size and height.

Third, satellite data can provide satisfactory urban morphology information in generating high-quality UCMap for urban climate studies. These results show an overall prediction error of 14% for the estimated UCMap using satellite data, meaning that more than 86% of the actual values were correctly predicted with satellite data.

6.2. Scale effect

Spatial scale of urban morphological information is an important consideration for practical applications. The spatial scale's influence on the accuracy of estimated results was tested in this study at resolutions of 100, 200, 300, 400, 500, and 600 m.

Fig. 11 shows the R square results of different parameters at different spatial resolutions, demonstrating that R square values grow as the spatial scale grows coarser. This finding indicates that better prediction accuracy can be achieved using a coarse spatial scale. For example, we obtained a fitting R square for SVF of 0.93 at a coarse spatial resolution of 500 m, which was much better than the fitting accuracy

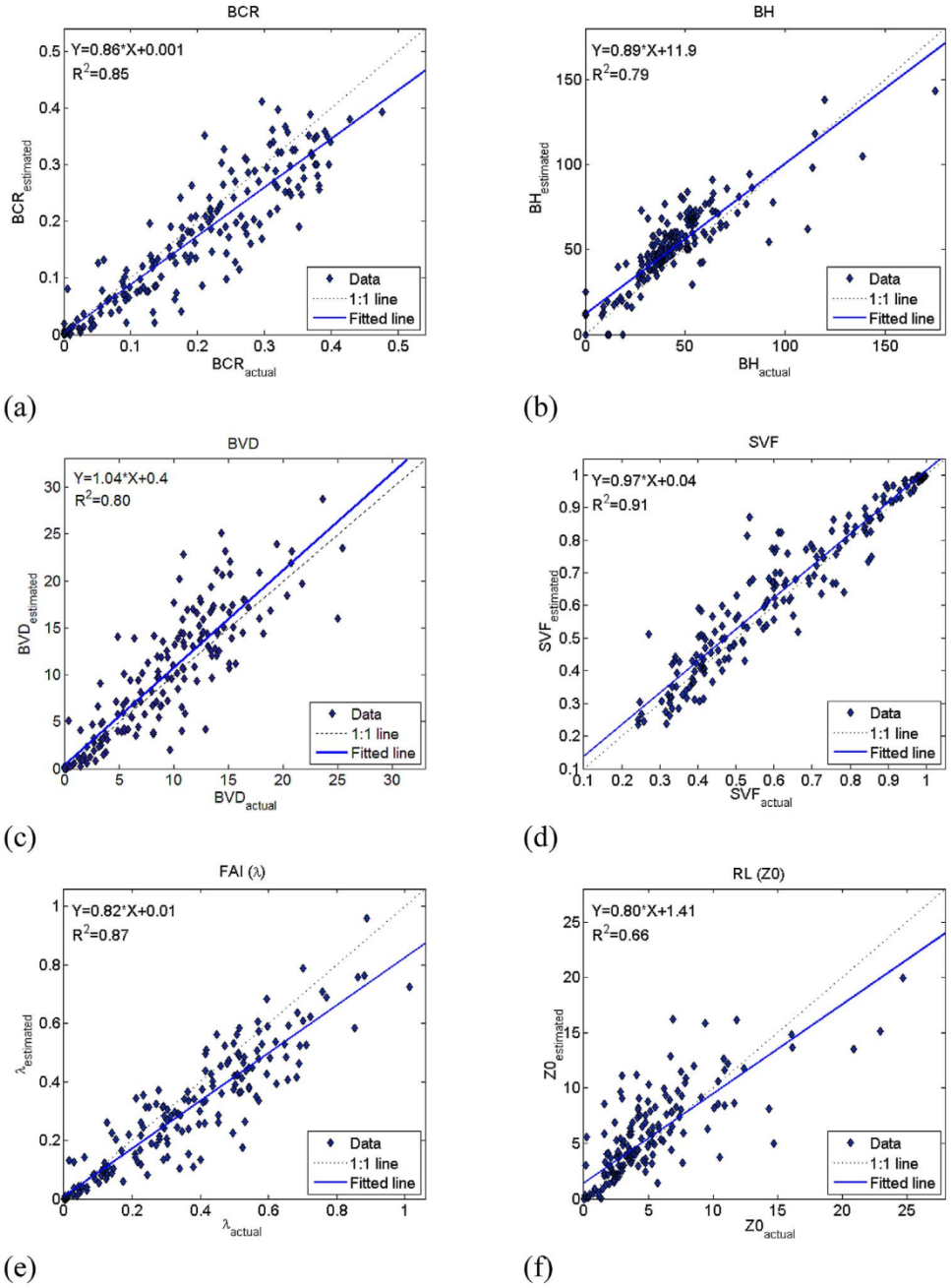

Fig. 7. Scatter plots of actual and estimated morphological parameters for: (a) BCR; (b) BH; (c) BVD; (d) SVF; (e) FAI; (f) RL.

Table 2
Relation between satellite-derived urban morphological parameters and actual parameters (average size: 300m*300m) from a real 3D urban model, including the overall prediction accuracy.

Parameter Name	Regression models (X: actual; Y: estimated)	R square (R^2)	Significance (5%)	RMSE
BCR	Y = 0.86*X + 0.001	R^2 = 0.85	yes	0.05
BH	Y = 0.89*X + 11.9	R^2 = 0.79	yes	11.8
BVD	Y = 1.04*X + 0.4	R^2 = 0.80	yes	3.07
SVF	Y = 0.97*X + 0.04	R^2 = 0.91	yes	0.07
FAI	Y = 0.82*X + 0.01	R^2 = 0.87	yes	0.1
RL	Y = 0.80*X + 1.41	R^2 = 0.66	yes	1.62

achieved with an R square of 0.87 for the same parameter at a fine spatial resolution of 100 m.

Thus, if fine spatial resolution is not required for urban morphological parameters, a coarser resolution (e.g., 600 m) can be used to provide better prediction accuracy. To achieve better prediction accuracy while preserving high spatial resolution, a spatial scale of 200–300 m is recommended when satellite data are used to generate the morphological parameters.

6.3. Implications

6.3.1. Impact on urban climatic conditions

To evaluate the impact of satellite-derived morphology on urban climatic conditions, wind and thermal environments were simulated and evaluated using a satellite-derived building model. The PALM model developed by Raasch and Schr & ter (2001) was employed to simulate urban wind environment by considering pedestrian level (2 m) wind velocity ratio, while the SOLWEIG model developed by Lindberg, Holmer, and Thorsson (2008) was used to simulate urban thermal environment by considering mean radiant temperature (Tmrt) of a typical

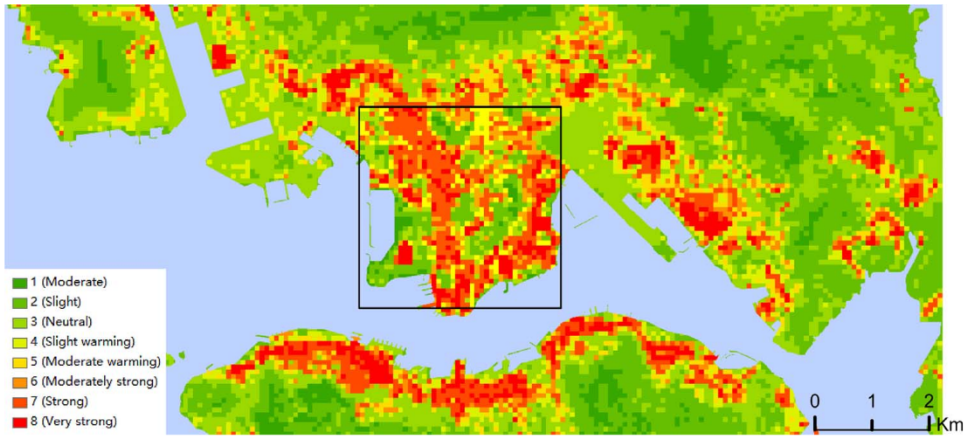

Fig. 8. Urban climatic map generated from actual GIS data.

summer time of year 2014. Settings of the LES model for this study were the same as those used by Wang, Xu, and Ng (2016); details for the settings of the SOLWEIG model are provided in Lau, Ren, Ho, and Ng (2016). To reduce computation time, satellite-derived and actual building data of the same 2 km by 2 km area were used to conduct the simulations. For comparison purposes, model-based urban wind and thermal simulations based on actual building data were also given.

Fig. 12(a) shows the computed wind environment using the PALM model, in which pedestrian-level wind velocity ratios (VRs) at the input wind direction from the southwest (prevailing direction) were simulated based on the satellite-derived urban morphology data, while Fig. 12(b) shows the computed VR using actual 3D urban morphology. Based on the SOLWEIG model, the thermal environment during a typical summer was simulated. Fig. 13(a) shows the Tmrt result using satellite-derived building morphology, while Fig. 13(b) shows the computed Tmrt result based on actual 3D urban morphology.

Scatter plots were used to indicate the relationship between computed wind and thermal environments based on satellite-based and actual building morphology data, with the x-coordinates representing the results of the actual GIS data and y-coordinates representing the results of the satellite-derived data. Fig. 14(a) and (b) shows the scatter plots for both VR and Tmrt simulations, which show that all points are along the 1:1 line, indicating that the simulated climatic conditions with satellite-derived data are consistent with the results based on actual building data.

Furthermore, a regression model was used to ascertain the relationship between the simulated wind and thermal conditions using satellite-derived and actual building models. R squares of the fitting models for VR and Tmrt simulations were 0.80 and 0.94, while RMSEs for both simulations were 0.02 and 0.6, respectively. Given the average VR and Tmrt simulations of 0.09 and 36.8 for this study area, it can be

Table 3
Average absolute difference (AAD) and correlation coefficients (CC) between the satellite-derived urban climatic map and the actual map from real urban GIS data.

Indices	AAD	AAD_%	CC
Accuracy	0.67	14%	0.88

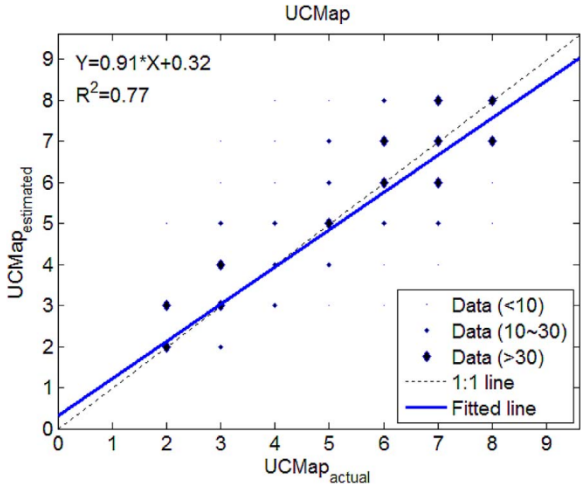

Fig. 10. Accuracy validation with x coordinate reflects values from the actual GIS data; y coordinate reflects values from the satellite data.

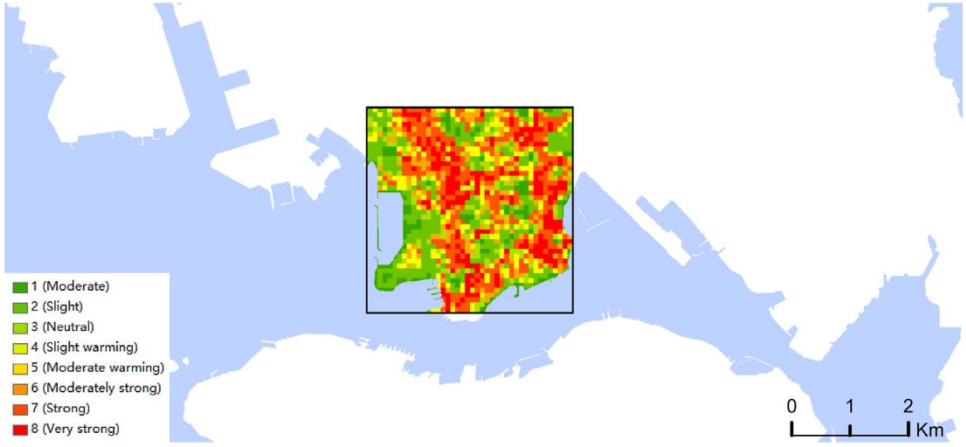

Fig. 9. Urban climatic map generated from satellite data.

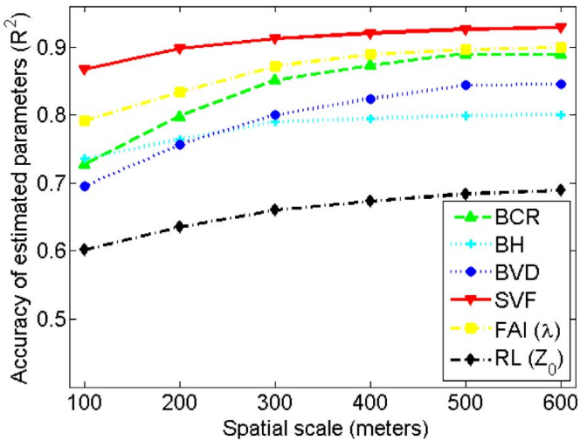

Fig. 11. Relationship between spatial scale and accuracy of satellite-derived morphological parameters measured by R-squared value from linear regression model.

inferred that the overall prediction errors of the simulated wind and thermal conditions based on satellite-derived urban morphology were 22% and 2%.

Based on the outdoor thermal comfort studies conducted by Ng et al. (2011) and Chen et al. (2012), an acceptable wind difference of 0.5 m/s (equivalent to a wind velocity ratio difference of 0.05) and a maximum acceptable temperature difference of 1.5 °C were recommended under mild conditions. Thus, the impact of satellite-derived urban morphology in urban wind and thermal conditions (with VR of 0.02 and Tmrt of 0.6 °C) is far below risk levels (with a VR of 0.06 and Tmrt of 1.5 °C), indicating that the satellite-derived urban morphology data meets the requirements of urban climate studies, with low impact—far below risk levels—on urban thermal and wind conditions.

6.3.2. Implications for urban climatic map studies

The Urban Climatic Map (UCMap) is an important tool for illustrating climatic understanding in two-dimensional maps used for sustainable urban planning with climatic concerns (HKPD, 2012; Ren et al., 2011). To date, over 30 countries have conducted urban climate studies to support regional urban planning (Acero et al., 2013; Ren et al., 2011). Major efforts in this field have mainly occurred in already-developed areas (Ng & Ren, 2015); however, urbanization processes occur rapidly in developing countries. Without reliable urban morphological data, it has been difficult to include urban climatic map studies or urban climatic applications in local urban development. This study demonstrates to climatologists and planners that a satellite-based method can generate highly accurate urban morphology data for urban climatic map studies. Because it is inexpensive, this method can be introduced and widely implemented in developing countries for their urban climatic map studies.

6.3.3. Implications for WUDAPT

The World Urban Database and Access Portal Tools (WUDAPT, www.wudapt.org) is an initiative to collect data on the forms and functions of cities worldwide to help develop their own heat-adaptation plans (Bechtel et al., 2015; Ching et al., 2009; Mills et al., 2015; See, Mills, & Ching, 2015). The WUDAPT helps climatologists and urban experts to use free satellite sources including Landsat 8, Google Earth, and free SAGA to create local climate zones (Mills et al., 2015). WUDAPT contains three approach levels. The Level 0 method is the initial step to quickly assembling data for creating and mapping LCZ classes. However, the available free data sources for certain types of LCZ may suffer low accuracy. Meanwhile, for detailed modeling setting and further urban climatic studies, Level 1 and Level 2 require more precise and reliable urban morphological data. Thus, the satellite-based methods used in this study can provide a solution to this problem.

Currently, urban climate models (e.g., WRF/urban modeling system) have been widely utilized in simulations of urban climatic conditions to explore urban climatic issues (Chen et al., 2011; Zhang, Gao, Wang, & Chen, 2010). However, the default input data of urban climate models (e.g., WRF/urban modeling systems) contain only three different urban classes (commercial, industrial, and high or low residential areas), which are too coarse to provide accurate simulation results (e.g., air pollution) at the city level (Salamanca et al., 2011). Scientists have investigated the use of more precise urban morphology data as the input in urban climate models, as well as discussing the development of better parameterization schemes for specific cities (Ching et al., 2009; Wang and Dai, 2015). The WUDAPT level-2 data products developed with the approach proposed in this study can provide urban morphological parameters of a finer scale, or a better parameterization scheme to provide better simulation results in urban climate research (Ching et al., 2009).

7. Conclusions

Urban morphological information is essential for urban climatic applications, urban planning and design, and the improvement of living environments in future cities. Particularly in developing countries, there is a need for high-accuracy and reliable urban morphological

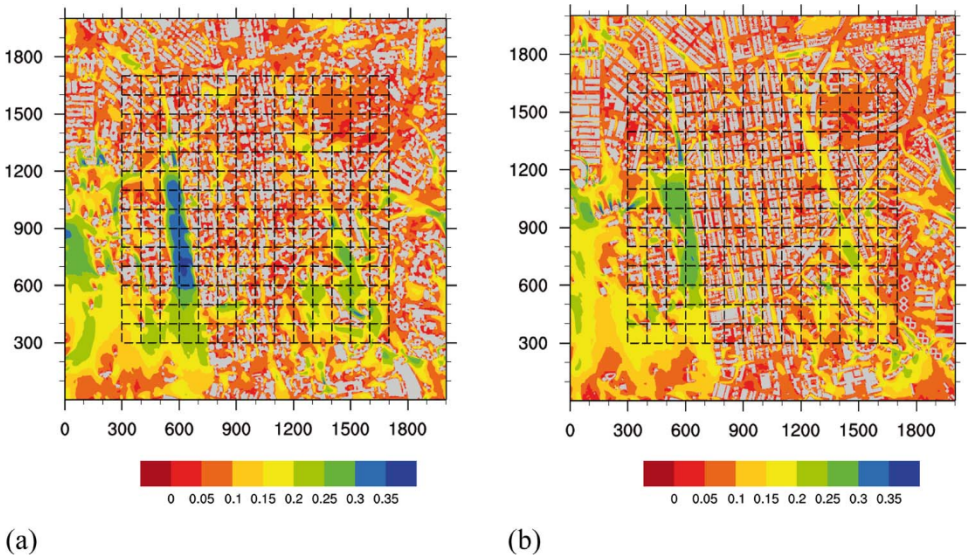

Fig. 12. Velocity Ratio (VR) Simulations based on PALM-LES model using (a) satellite-derived building morphology, and (b) actual building morphology.

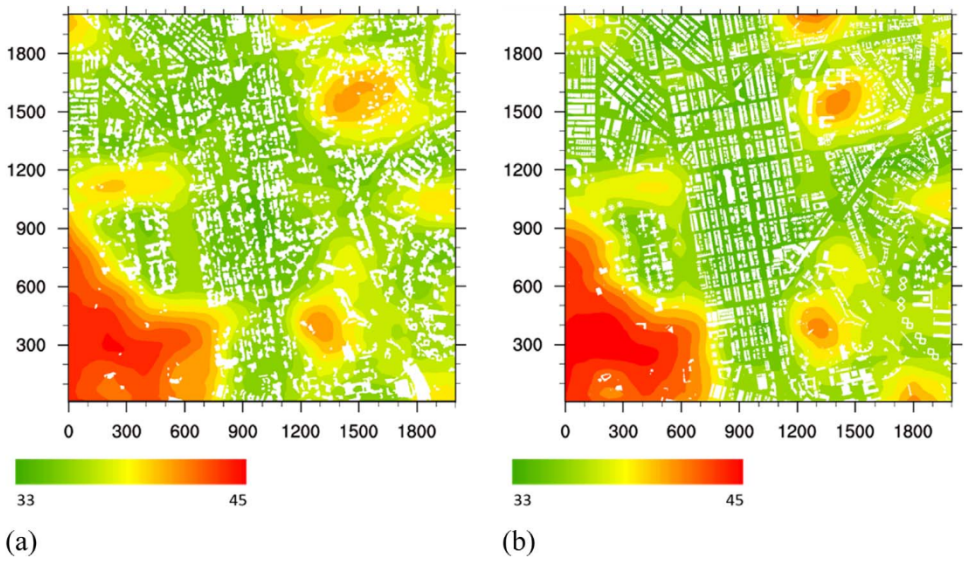

Fig. 13. Mean Radiant Temperature (Tmrt) Simulations based on SOLWEIG model using (a) satellite-derived building morphology, and (b) actual building morphology.

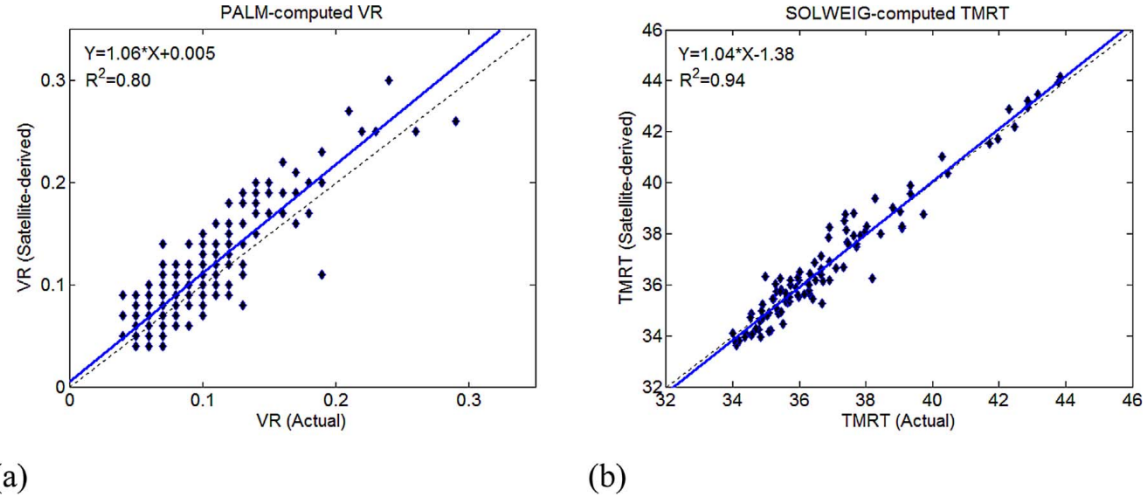

Fig. 14. Scatter plots of simulated urban climactic conditions based on satellite-based or actual building morphology, with x coordinates resulting from actual GIS data and y coordinates resulting from satellite-derived data. (a) Wind velocity; (b) mean radiant temperature.

information for their urban climatic application studies and urban development. To that end, this study has developed a novel satellite-based (yet inexpensive) approach proven to be suitable for obtaining 3D urban morphological information. Two types of satellite data—high-resolution World-view satellite data and Terra-SAR—were used. Six of the most widely used urban morphological parameters for urban climate studies were systematically tested in this study, namely BCR, BH, BVD, SVF, FAI, and RL. Validation results showed that all of the retrieved parameters achieved a high prediction accuracy, suggesting that low-cost satellite data can produce promising urban morphological parameters to support urban climate studies. Moreover, a highly consistent performance was found for satellite-derived morphological parameters and actual parameters when both datasets were applied to urban climate studies, whether for urban climatic mapping or for intra-urban temperature and wind ventilation analyses. Thus, satellite-based urban morphological parameters can be effectively applied in urban climate studies.

This research also reveals that satellite-based technology tends to underestimate building footprints in high-density urban areas, while overestimating the heights of low buildings. These inconsistencies lead to large uncertainties of the estimation of some morphological parameters (e.g., BVD and RL) in high-density urban areas. The approach proposed here is straightforward, and opens up new possibilities for using satellite-driven urban morphological data for urban climatic applications like the urban climatic map and WUDAPT, especially in developing countries where urban morphological data are unavailable. Because all generated data are managed in GIS, they can also form the collaboration basis for further building simulation and urban climate modeling.

Acknowledgments

This study was supported by the Hong Kong Research Grants Council General Research Fund 14611015, A perspective (1960-2030) of Hong Kong's urban development and urban climate – a historical context for future actions) and the National Natural Science Foundation of China (41601356).

References

Acero, J. A., Arrizabalaga, J., Kupski, S., & Katzschner, L. (2013). Deriving an Urban Climate Map in coastal areas with complex terrain in the Basque Country (Spain). *Urban Climate*, *4*, 35–60.

Bechtel, B., Alexander, P. J., Böhner, J., Ching, J., Conrad, O., Feddema, J., ... Stewart, I. (2015). Mapping local climate zones for a worldwide database of the form and function of cities. *ISPRS International Journal of Geo-Information*, *4*(1), 199–219.

Burian, S. J., Velugubantla, S. P., & Brown, M. J. (2002). *Morphological analyses using 3D building databases*. Phoenix, Arizona: Los Alamos National Laboratory [LA-UR-02-

6726].
Chen, F., Kusaka, H., Bornstein, R., Ching, J., Grimmond, C. S. B., Grossman-Clarke, S., ... Sailor, D. (2011). The integrated WRF/urban modelling system: Development, evaluation, and applications to urban environmental problems. *International Journal of Climatology*, *31*(2), 273–288.
Chen, L., Ng, E., An, X., Ren, C., Lee, M., Wang, U., & He, Z. (2012). Sky view factor analysis of street canyons and its implications for daytime intra-urban air temperature differentials in high-rise, high-density urban areas of Hong Kong: A GIS-based simulation approach. *International Journal of Climatology*, *32*(1), 121–136.
Ching, J., Brown, M., Burian, S., Chen, F., Cionco, R., Hanna, A., ... Williams, D. (2009). National urban database and access portal tool, NUDAPT. *Bulletin of American Meteorological Society*, *90*(8), 1157–1168.
Ching, J. K. S. (2013). A perspective on urban canopy layer modeling for weather: Climate and air quality applications. *Urban Climate*, *3*, 13–39.
Coceal, O., & Belcher, S. E. (2005). Mean winds through an inhomogeneous urban canopy. *Boundary-Layer Meteorology*, *115*(1), 47–68.
Colin-Koeniguer, E., & Trouve, N. (2014). Performance of building height estimation using high-Resolution PolInSAR images. *IEEE Transactions on Geoscience and Remote Sensing*, *52*(9), 5870–5879.
Eckert, S., & Hollands, T. (2010). Comparison of automatic DSM generation modules by processing IKONOS stereo data of an urban area. *IEEE Journal of Selected Topics in Applied Earth Observations and Remote Sensing*, *3*(2), 162–167.
Eliasson, I. (2000). The use of climate knowledge in urban planning. *Landscape and Urban Planning*, *48*, 31–44. http://dx.doi.org/10.1016/S0169-2046(00)00034-7.
Gál, T., Lindberg, F., & Unger, J. (2009). Computing continuous sky view factors using 3D urban raster and vector databases: comparison and application to urban climate. *Theoretical and Applied Climatology*, *95*(1–2), 111–123.
Gál, T., & Unger, J. (2009). Detection of ventilation paths using high-resolution roughness parameter mapping in a large urban area. *Building and Environment*, *44*(1), 198–206.
Givoni, B. (1998). *Climate considerations in building and urban design*. New York: Van Nostrand Reinhold.
Grimmond, C. S. B., Potter, S. K., Zutter, H. N., & Souch, C. (2001). Rapid methods to estimate sky-view factors applied to urban areas. *International Journal of Climatology*, *21*(7), 903–913.
Grimmond, S. (2007). Urbanization and global environmental change: Local effects of urban warming. *The Geographical Journal*, *173*(1), 83–88.
Höppe, P. (2008). Rising natural catastrophe losses — What is the role of climate change? In B. Hansjürgens, & R. Antes (Eds.), *Economics and managment of climate change: Risks, mitigation and adaptation* (pp. 13–22). Springer.
HKPD (Hong Kong Planning Department) (2012). *Final report, urban climatic map and standards for wind environment-feasibility study*Planning Department, Hong Kong Government. Available at: http://www.pland.gov.hk/pland_en/p_study/prog_s/ucmapweb/ucmap_project/content/reports/final_report.pdf.
Hansen, F. V. (1993). *Surface roughness lengths (No. ARL-TR-61)*. ARMY RESEARCH LAB WHITE SANDS MISSILE RANGE NM.
Krazter, P. A. (1956). *The climate of cities*. Braunschweig: Friedr. Vieweg and Sohn.
Kubota, T., Miura, M., Tominaga, Y., & Mochida, A. (2008). Wind tunnel tests on the relationship between building density and pedestrian-level wind velocity: Development of guidelines for realizing acceptable wind environment in residential neighborhoods. *Building and Environment*, *43*(10), 1699–1708.
Landsberg, H. E. (1970). *Climates and urban planning, urban climate*. Geneva, Switzerland: World Meteorological Organization, 366–377 Technical No. 108.
Lau, K. K. L., Ren, C., Ho, J., & Ng, E. (2016). Numerical modelling of mean radiant temperature in high-density sub-tropical urban environment. *Energy and Buildings*, *114*, 80–86.
Lindberg, F., Holmer, B., & Thorsson, S. (2008). SOLWEIG 1. 0–Modelling spatial variations of 3D radiant fluxes and mean radiant temperature in complex urban settings. *International Journal of Biometeorology*, *52*(7), 697–713.
Ma, P., Lin, H., Lan, H., & Chen, F. (2015). On the performance of reweighted minimization for tomographic SAR imaging. *IEEE Geoscience and Remote Sensing Letters*, *12*(4), 895–899.
Macdonald, R. W., Griffiths, R. F., & Hall, D. J. (1998). An improved method for the estimation of surface roughness of obstacle arrays. *Atmospheric Environment*, *32*(11), 1857–1864.
Matuschek, O., & Matzarakis, A. (2010). *Estimation of sky view factor in complex environment as a tool for applied climatological studies*, *vol. 20*, Freiburg: Berichte des Meteorologischen Instituts der Albert-Ludwigs-Universität, 534–539.
Middel, A., Häb, K., Brazel, A. J., Martin, C. A., & Guhathakurta, S. (2014). Impact of urban form and design on mid-afternoon microclimate in Phoenix Local Climate Zones. *Landscape and Urban Planning*, *122*, 16–28.
Mills, G., Cleugh, H., Emmanuel, R., Endlicher, W., Erelle, E., McGranahan, G., ... Steemer, K. (2010). Climate information for improved planning and management of mega cities (Needs perspective). *Procedia Environmental Sciences*, *1*, 228–246. http://dx.doi.org/10.1016/j.proenv.2010.09.015.
Mills, G., Ching, J., See, L., Bechtel, B., & Foley, M. (2015). An introduction to the WUDAPT project. *9th international conference on urban climate*.
Ng, E., & Ren, C. (2015). *The urban climatic map: A methodology for sustainable urban planning*. Abingdon, Oxon; New York, NY: Routledge.
Ng, E., Yuan, C., Chen, L., Ren, C., & Fung, J. C. (2011). Improving the wind environment in high-density cities by understanding urban morphology and surface roughness: A study in Hong Kong. *Landscape and Urban Planning*, *101*(1), 59–74.
Ng, E., Ren, C., & Katzschner, L. (2012). Urban climatic mapping in Hong Kong. *Journal of Heat Island Institute International*, *7*(2), 55–64.
Ng, E. (2009). Policies and technical guidelines for urban planning of high-density cities–air ventilation assessment (AVA) of Hong Kong. *Building and Environment*, *44*(7), 1478–1488.
Ng, E. (2012). Towards planning and practical understanding of the need for meteorological and climatic information in the design of high-density cities: A case-based study of Hong Kong. *International Journal of Climatology*, *32*(4), 582–598. http://dx.doi.org/10.1002/joc.2292.
Oke, T. R. (1973). City size and the urban heat island. *Atmospheric Environment*, *7*, 769–779.
Oke, T. R. (1981). Canyon geometry and the nocturnal urban heat island: Comparison of scale model and field observations. *International Journal of Climatology*, *1*(3), 237–254.
Oke, T. R. (1984). Towards a prescription for the greater use of climatic principles in settlement planning. *Energy and Buildings*, *7*, 1–10.
Oke, T. R. (1988). Street design and urban canopy layer climate. *Energy and Buildings*, *11*, 103–113.
Oke, T. R. (2003). Green plot ratio: An ecological measure for architecture and urban planning. *Landscape and Urban Planning*, *63*, 197–211.
Petralli, M., Massetti, L., Brandani, G., & Orlandini, S. (2014). Urban planning indicators: Useful tools to measure the effect of urbanization and vegetation on summer air temperatures. *International Journal of Climatology*, *34*(4), 1236–1244.
Raasch, S., & Schröter, M. (2001). PALM–a large-eddy simulation model performing on massively parallel computers. *Meteorologische Zeitschrift*, *10*(5), 363–372.
Razak, A. A., Hagishima, A., Ikegaya, N., & Tanimoto, J. (2013). Analysis of airflow over building arrays for assessment of urban wind environment. *Building and Environment*, *59*, 56–65.
Ren, C., Ng, E. Y. Y., & Katzschner, L. (2011). Urban climatic map studies: A review. *International Journal of Climatology*, *31*(15), 2213–2233.
Ren, C., Spit, T., Lenzholzer, S., Yim, H. L. S., Heusinkveld, B., van Hove, B., ... Katzschner, L. (2012). Urban climate map system for Dutch spatial planning. *International Journal of Applied Earth Observation and Geoinformation*, *18*, 207–221.
Roth, M. (2007). Review of urban climate research in (sub) tropical regions. *International Journal of Climatology*, *27*(14), 1859–1873.
Salamanca, F., Martilli, A., Tewari, M., & Chen, F. (2011). A study of the urban boundary layer using different urban parameterizations and high-resolution urban canopy parameters with WRF. *Journal of Applied Meteorology and Climatology*, *50*(5), 1107–1128.
Salehi, B., Zhang, Y., Zhong, M., & Dey, V. (2012). Object-based classification of urban areas using VHR imagery and height points ancillary data. *Remote Sensing*, *4*(8), 2256–2276.
See, L., Mills, G., & Ching, J. (2015). Climate modelling: Community initiative tackles urban heat. *Nature*, *526*, 43. http://dx.doi.org/10.1038/526043b.
Sportouche, H., Tupin, F., & Denise, L. (2011). Extraction and three-dimensional reconstruction of isolated buildings in urban scenes from high-resolution optical and SAR spaceborne images. *IEEE Transactions on Geoscience and Remote Sensing*, *49*(10), 3932–3946.
Steeneveld, G. J., Koopmans, S., Heusinkveld, B. G., & Theeuwes, N. E. (2014). Refreshing the role of open water surfaces on mitigating the maximum urban heat island effect. *Landscape and Urban Planning*, *121*, 92–96.
Stewart, I. D., & Oke, T. R. (2012). Local climate zones for urban temperature studies. *Bulletin of the American Meteorological Society*, *93*(12), 1879–1900.
Svensson, M. K. (2004). Sky view factor analysis–implications for urban air temperature differences. *Meteorological Applications*, *11*(03), 201–211.
UNFPA (2015). *The state of world population. World population prospects: The 2015 revision*. United Nations Population Fund. United Nations Population Division.
Wang, X., & Dai, W. (2015). Development of fine-scale urban canopy parameters in Guangzhou city and its application in the WRF-Urban model. *9th international conference on urban climate*.
Wang, W., Xu, Y., & Ng, E. (2016). Application of large-eddy simulations in evaluating ventilation over 3D building data retrieved from satellite images. *11th international conference on urban physics*.
Wegner, J. D., Ziehn, J. R., & Soergel, U. (2014). Combining high-resolution optical and InSAR features for height estimation of buildings with flat roofs. *IEEE Transactions on Geoscience and Remote Sensing*, *52*(9), 5840–5854.
Wendell Cox Consultancy (2015). *World megacities: Urban areas with more than 10,000,000 population, demographia world urban areas*. [from:] http://www.demographia.com/db-megacity.pdf.
Xu, Y., Ma, P., Ng, E., & Lin, H. (2015). Fusion of WorldView-2 stereo and multi-temporal TerraSAR-X images for building height extraction in urban areas. *IEEE Geoscience and Remote Sensing Letters*, *12*(8), 1795–1799.
Yoshie, R., Mochida, A., & Tominaga, Y. (2006). CFD prediction of wind environment around a high-rise building located in an urban area. *Proceedings of the fourth international symposium on computational wind engineering (CWE2006)* (pp. 16–19).
Yu, B., Liu, H., Wu, J., Hu, Y., & Zhang, L. (2010). Automated derivation of urban building density information using airborne LiDAR data and object-based method. *Landscape and Urban Planning*, *98*(3), 210–219.
Yuan, C., & Ng, E. (2012). Building porosity for better urban ventilation in high-density cities–A computational parametric study. *Building and Environment*, *50*, 176–189.
Zeng, C., Wang, J., Zhan, W., Shi, P., & Gambles, A. (2014). An elevation difference model for building height extraction from stereo-image-derived DSMs. *International Journal of Remote Sensing*, *35*(22), 7614–7630.
Zhang, N., Gao, Z., Wang, X., & Chen, Y. (2010). Modeling the impact of urbanization on the local and regional climate in Yangtze River Delta, China. *Theoretical and Applied Climatology*, *102*(3–4), 331–342.
Zhou, G., & Zhou, X. (2014). Seamless fusion of LiDAR and aerial imagery for building extraction. *IEEE Transactions on Geoscience and Remote Sensing*, *52*(11), 7393–7407.
d'Angelo, P., Lehner, M., Krauss, T., Hoja, D., & Reinartz, P. (2008). Towards automatedha DEM generation from high resolution stereo satellite images. *International Society for Photogrammetry and Remote Sensing*, *37*(B4), 1137–1342.